



OPEN

DATA DESCRIPTOR

A new open, high-resolution, multishell, diffusion-weighted imaging dataset of the living squirrel monkey

Thomas Orset ^{1,2,✉}, Julie Royo ^{1,2}, Mathieu David Santin ^{3,5}, Pierre Pouget ^{1,2,5} & Michel Thiebaut de Schotten ^{1,4,5}

Although very well adapted to brain study, Magnetic Resonance Imaging (MRI) remains limited by the facilities and capabilities required to acquire data, especially for non-human primates. Addressing the data gaps resulting from these limitations requires making data more accessible and open. In contempt of the regular use of *Saimiri sciureus* in neuroscience research, *in vivo* diffusion has yet to be openly available for this species. Here we built and made openly available a unique new resource consisting of a high-resolution, multishell diffusion-weighted dataset in the anesthetized *Saimiri sciureus*. The data were acquired on 11 individuals with an 11.7T MRI scanner (isotropic resolution of 400 μm^3). This paper presents an overview of our dataset and illustrates some of its possible use through example analyses. To assess the quality of our data, we analyzed long-range connections (whole-brain tractography), microstructure (Neurite Orientation Dispersion and Density Imaging), and axon diameter in the corpus callosum (ActiveAx). Constituting an essential new resource for primate evolution studies, all data are openly available.

Background & Summary

Since the 1960s, the common squirrel monkey (*Saimiri sciureus*) has been used as a model in a wide range of biomedical fields, including cardiovascular physiology, pharmacology, genetics, and, to a great extent, neuroscience¹. Squirrel monkeys are small non-human primates part of the Haplorhini order and Cebidae family and, consequently, are closer to humans than Marmosets or Three shrews. They show phylogenetic, anatomic, functional, and behavioral similarities with humans, making them very relevant to clinical neuroscience².

Squirrel monkeys can be tested on various behavioral tasks adapted from rodents or non-human primates, including reaching, grasping, and inhibitory motor tasks³. They express hand preference in specific tasks⁴. Like macaques, they can achieve oculomotor tasks such as saccades or smooth pursuit tasks⁵. Working memory is another well-developed function in squirrel monkeys, comparable to macaques and humans⁶ and superior to marmosets⁷. Exploring the squirrel monkey's brain can shed light on the mechanisms supporting primates' functions and their evolutions as well as potentially reveal new targets for treating human brain dysfunctions^{8,9}.

The squirrel monkey's brain is more prominent (~22572 mm³) and has a higher neo-cortex/all brain ratio (69%) than the marmoset's and the tree shrew's respectively (~7241 mm³ and 60%) and (~3495 mm³ and ~27%)^{10,11}. The squirrel monkey's brain presents marked sulci, such as the arcuate sulcus. Finally, despite their larger brain than marmosets, squirrel monkeys' global size remains suitable for small-bore MRI scanners working at ultra-high fields to peer into the anatomical and functional micro-structures of the living brain.

The relationship between anatomy and function is complex. From the microstructure to the large-scale network of task-related activations, investigating the brain circuitry is an elegant way to bridge anatomy with function¹². Diffusion-weighted magnetic resonance imaging (DWI)¹³ is the only method sensitive to the orientation

¹Brain Connectivity and Behaviour Laboratory, Sorbonne University, Paris, France. ²Sorbonne University, Inserm U1127, CNRS UMR7225, UM75, ICM, Movement Investigation and Therapeutics Team, Paris, France. ³ICM, Centre de NeuroImagerie de Recherche – CENIR, Paris, France. ⁴Groupe d'Imagerie Neurofonctionnelle, Institut des Maladies Neurodégénératives-UMR 5293, CNRS, CEA University of Bordeaux, Bordeaux, France. ⁵These authors contributed equally: Mathieu David Santin, Pierre Pouget, Michel Thiebaut de Schotten. ✉e-mail: orset.thomas@gmail.com

| Animal Identification | Age (years) | Weight (g) |
|-----------------------|-------------|------------|
| Agi | 7 | 730 |
| Asa | 9 | 650 |
| Cor | 6 | 790 |
| Ena | 7 | 770 |
| Gai | 8 | 760 |
| Gal | 10 | 795 |
| Iye | 8 | 800 |
| Kan | 8 | 790 |
| Maz | 6 | 790 |
| Ros | 9 | 740 |
| Wyn | 7 | 675 |

Table 1. Age and weight details at the date of MRI for the 11 subjects available to date. Subjects were all adult females aged 6 to 10 years old and weighing 754.5 ± 51 g.

and fibers in the living brain. Combined with tractography, it reveals the close relationship or connection between brain regions¹⁴. DWI is a non-invasive Magnetic Resonance Imaging (MRI) method that can estimate the orientation of the diffusion of water molecules in any tissue. Because water molecules diffuse preferentially along and within axons rather than across them, tractography can produce plausible macroscopic white matter trajectories by piecing together local estimates of diffusion orientation^{15–18}.

DWI can also be employed to estimate microstructural features such as tract-specific integrity¹⁹, neurite density²⁰ and axonal diameter²¹, amongst others. Such connectivity metrics are optimal in the living brain as death quickly degrades the fragile white matter architecture²². Death affects mean diffusivity due to dehydration, protein cross-linking²³ or decreased permeability²⁴. Accordingly, diffusion in *ex vivo* models decreases and is less sensitive^{25,26}. Temperature changes also alter diffusion properties in a compartment-dependent manner²⁴. Further, long-term post-mortem brain conservation requires formalin fixation that is known to cause tissue shrinkage^{27,28}, potentially in a non-homogenous way, as previously reported in the mouse²⁹. Hence, the clinical relevance of DWI requires acquiring specimens *in vivo* for comparability to humans, in which proper perfusion and fixation are not feasible³⁰. Since DWI sequences can be expensive to implement and challenging to process, several groups offered open access to datasets in humans³¹, macaques^{32,33}, mice and other species^{34–37} to fuel progress in neurosciences. However, the absence of a living squirrel monkey DWI dataset hampers the progress of comparative models and prevents us from building comprehensive and accurate evolutionary trees of the brain.

Therefore, this paper summarizes the parameters and open access details to the first diffusion-weighted imaging dataset of the living squirrel monkey. We also provide codes, when available, preliminary results, and perspectives for future projects using this new resource.

Methods

Animals. Data were acquired from 11 adult female *Saimiri sciureus* between 6 and 10 years old at the imaging time, with an average weight of 754.5 ± 51 g (see Table 1 for individual details). All procedures were designed in association with the veterinarian team of the ICM Paris Brain Institute (agreement number B75-13-19), approved by the Regional Ethical Committee for Animal Experiments (Charles Darwin CE005 under the project reference APAFIS #21086-2019061415485300). Saimiris were housed in a social group within Paris Brain Institute (ICM) in a multi-compartment cage complex (17.5 m³) with structural and manipulable enrichments (ladders, platforms, hammock...) at constant temperature (24–26 °C), relative humidity (55%) and a 12 h light-darkness cycle. The animals had *ad libitum* access to water, and food was given three times a day, including commercial monkey chow, fruits, vegetables and other various enrichments (eggs, nuts, seeds, mealworms...).

Anesthesia. Anesthesia was induced with an intramuscular (IM) injection of Alfaxalone (3 mg/kg) and maintained with isoflurane during animal preparation. The subject received an intramuscular injection of Dexdomitor (0.5 mg/kg) and anesthesia was maintained with perfusion of Alfaxalone (12 mg/kg). Internal temperature and respiratory rate were monitored throughout the MRI sequences. After 2 hours in the scanner or if the respiratory rate rose over 60/min, Alfaxalone's flow rate was adjusted to 18 mg/kg to prevent awakening. A warm water flow maintained body temperature between 34.5 and 38.5 °C. From induction to awakening, anesthesia lasted 6 ± 0.5 hours.

Acquisitions parameters. Magnetic Resonance (MR) Images were acquired using a Biospec USR 117/16 (Bruker, Germany). Radiofrequency emission and signal reception was performed using a 72-mm birdcage transceiver (Bruker, Germany). Before image acquisition, the automatic shim was computed using the MAPSHIM routine on an ellipsoid that fits the whole squirrel monkey brain. The field map obtained after shimming was estimated at $72 \times 72 \times 72$ mm³ to perform later distortion correction. Diffusion-weighted images were then acquired using a Fat-Saturated 3D-DW segmented EPI sequence with the following parameters: 4 segments, TR/TE = 200/24 ms, Bandwidth = 600 kHz, Mtx = 160*160*128, FOV = 64.0*64.0*51.2 mm³ leading to an isotropic resolution of $400 \times 400 \times 400$ μm³. Diffusion gradient duration $\delta = 3$ ms and gradient separation $\Delta = 11$ ms. A total number of 100 non-collinear diffusion gradient directions were acquired using three different b-values: 2 000, 1 000, and 300 s/mm² with 64, 29, and 7 directions, respectively. Directions were generated offline on a sphere

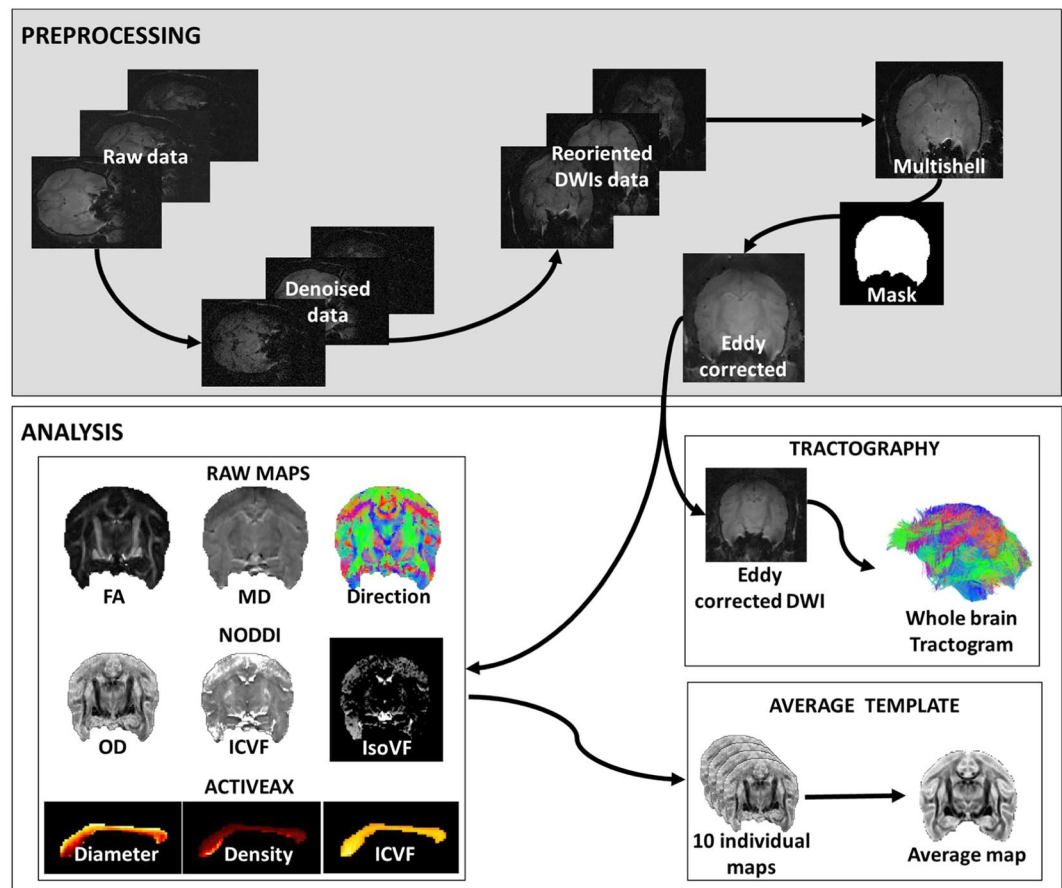


Fig. 1 Overview of the experimental workflow. The top frame summarizes preprocessing steps from raw data to eddy-corrected multishell. The bottom frame outlines analyses applied to the preprocessed images. Eddy-corrected images are used to generate maps and compute tractography. Maps of 10 individuals were used to create average templates⁴⁶. Note that the 11th individual data were acquired after the template creation and were not voluntarily excluded from the template creation.

using Carruyer's online Q-Space sampling tool³⁸. A total number of 8 non-diffusion weighted volumes were also acquired. The whole scanning time for this multi-shelled diffusion acquisition was 3h04 min per animal.

Preprocessing. Raw data were denoised, reoriented using ExploreDTI (www.exploredti.com), and the three b-values were merged (Fig. 1). A brain mask was generated and manually corrected with BrainSuite21a (www.brainsuite.org). Manual editing mainly consisted of extending the mask to the missing areas (due to a signal drop) or eroding the masked cerebrospinal fluid. Eddy currents-induced distortions and movement were corrected using the eddy tool from FSL.

Tractography. StarTrack (<http://www.mr-startrack.com>), together with Matlab, performed deterministic tractography analysis on multishell diffusion-weighted images by means of the damped Richardson Lucy Spherical deconvolution algorithm^{39,40} (Fig. 1). Spherical deconvolution parameters were set to ALFA = 2, iterations = 1000, $n = 0.001$, and $r = 8$. Whole brain deterministic tractography was performed using two runs of the M-Euler algorithm, with an absolute threshold of 0.005, step size of 0.4 mm, angle threshold of 35° and min and max streamline length of 8 and 100 mm, respectively. Manual tractography dissections were performed on the monkey Gal using Trackvis (www.trackvis.org) to demonstrate feasibility.

Models fitting. DWI can shed light on advanced microstructural information through specific models.

For instance, neurite orientation dispersion and density imaging (NODDI) estimates the complexity of dendrites and axons based on diffusion MRI data²⁰ (Fig. 1). It relies on three sub-model for intracellular, extra-cellular and cerebrospinal fluid (CSF) compartments. NODDI analyses provide maps of isometric volume fraction in CSF, intracellular volume fraction, and orientation dispersion (OD). The latter is a surrogate for neurite dispersion and synaptic complexity. Additionally, ActiveAx is a model used to calculate an orientationally invariant index of axon diameter and density⁴¹. Accordingly, we applied both models to the multishell dataset (B300, B1000, and B2000) after eddy current correction. Note that for practical purposes, ActiveAx estimations focused on the corpus callosum's mid-section (delineated manually by the authors).

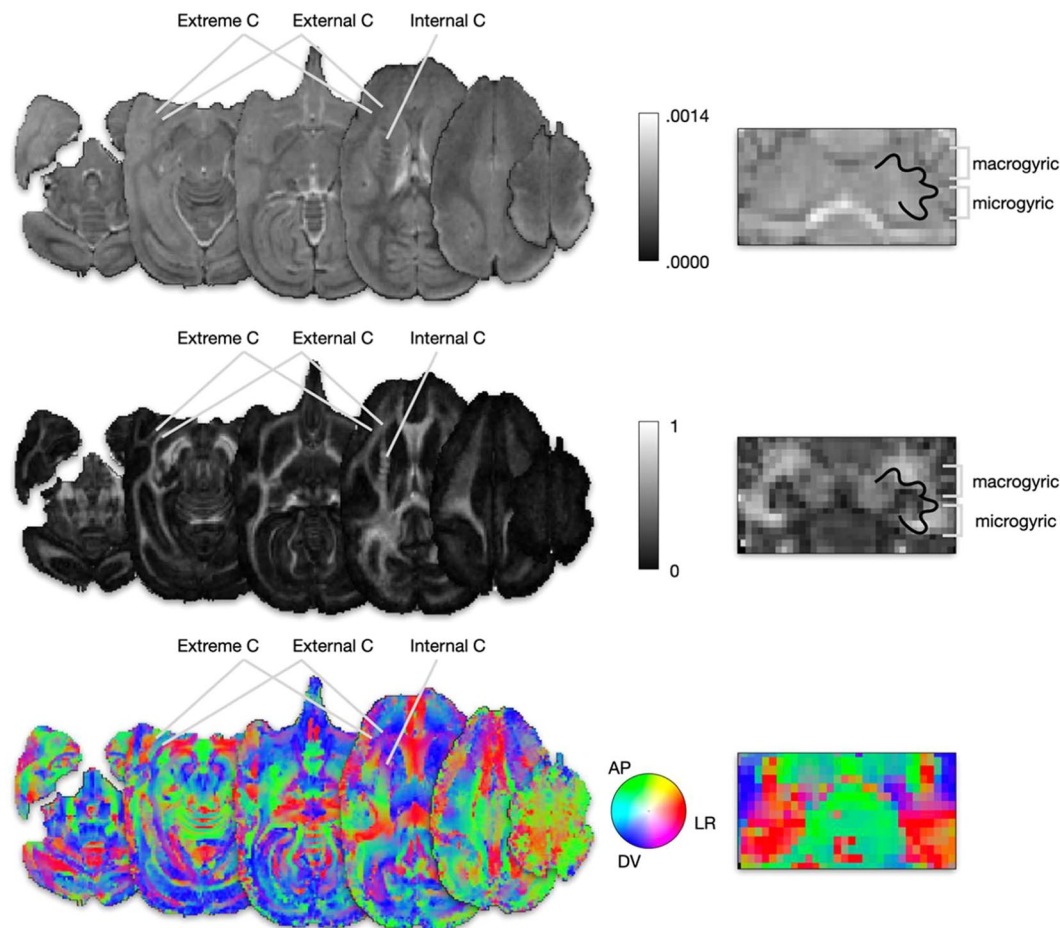


Fig. 2 Raw DWI maps $N = 1$. Axial (left panel) and coronal cerebellar (right panel) sections of (a) Mean Diffusivity, (b) Fractional Anisotropy and (c) RGB-encoded principal diffusion direction.

Data Records

The present dataset is stored on Figshare⁴² and a dedicated website, which will be regularly updated with additional data and analyses (<http://saimiri.bcblab.com>). We also opened a forum topic for questions and answers (<https://neurostars.org/t/squirrel-monkey-brain-mapping/24110>). The dataset comprise 11 folders, one per subject. Each subject folder contains one subfolder per b-value (2 000, 1 000, 300) and one subfolder for the B0 map registered to the diffusion data set. B-values folders comprise the raw image in .nii format, the b-vecs file in .txt format, and metadata in a .json file. B0 map folder includes B0 maps in .nii format and metadata in a .json file.

Technical Validation

We present here the first DWI open database of living squirrel monkeys' brains. To prompt the quality of our data we assessed the details of small anatomical structures, the quality of tractography dissections, the clarity of advanced multishell diffusion maps and the reproduction of classical expected brain patterns.

Figure 2 shows that despite the high resolution of the dataset, the signal was strong enough to make anatomical structures visible at the cortical and subcortical levels. Fractional anisotropy maps sharply delineated fine white matter anatomical landmarks such as the distinction between the extreme and external capsule, stripes in the internal capsule and the micro- and macrogyric architecture of the dentate nucleus⁴³.

Figure 3 shows the result of deterministic whole-brain tractography and examples of track dissection in a single subject. The whole tractogram (Fig. 3a) was composed of 554360 streamlines and allowed us to dissect thin fibers bundles such as the three SLF branches (Fig. 3b) as well as long-range connections, namely the inferior fronto-occipital fasciculus (Fig. 3c). The dissection of the inferior longitudinal fasciculus (Fig. 3d) has revealed a dense bundle with scattering in its posterior part.

The tractography of the squirrel monkey brain revealed a set of projection, association, and commissural connections quite comparable to humans. However, trained anatomists could spot obvious differences, including an indisputable disproportion between the ventral (inferior longitudinal fasciculus and inferior fronto-occipital fasciculus) and the dorsal (fronto-parietal system) when compared to humans^{44,45}. These differences reflect squirrel monkeys' relatively smaller frontal and parietal lobes than humans^{46–48}. Despite these disparities, the complexity of the squirrel monkey's circuitry was persuasive enough to investigate limbic, fronto-parietal, perisylvian and visual systems with potential translation to humans at the macroscopic level.

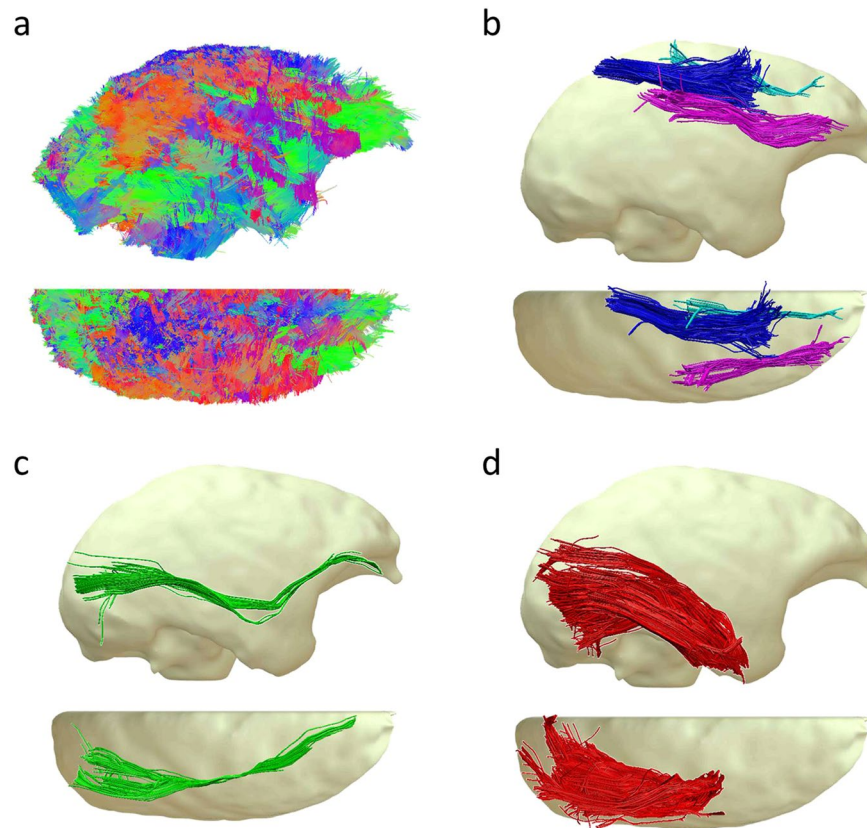


Fig. 3 Tractography dissection N = 1. (a) Right and top view of a whole brain tractogram composed of 554360 tracks. (b) The three branches of the Superior longitudinal fasciculus (SLF) I, II and III. (c) Inferior Longitudinal Fasciculus (IFOF). (d) Inferior Longitudinal Fasciculus (ILF).

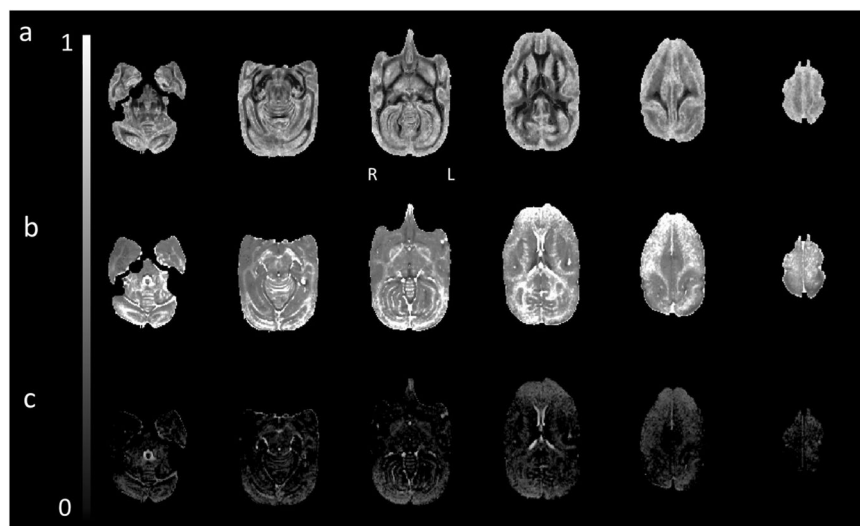


Fig. 4 NODDI analysis N = 1. Axial view from a whole brain NODDI analysis for (a) Orientation Dispersion, (b) Intracellular Volume Fraction, and (c) Isotropic (CSF) Volume Fraction.

Our multishell acquisition allows NODDI to estimate cerebrospinal volume fraction, neurite density, and dispersion at the microscopic level. Figure 4 displays the maps computed for a single subject. As expected, the Orientation Dispersion map (Fig. 4a) highlighted grey matter structures consistent with their complex axonal and dendritic (i.e., neurite) diffusion profile. Reversely, the map for intracellular volume fraction (Fig. 4b) displays consistent patterns with higher values in white matter. The third map for isotropic volume fraction (Fig. 4c) showed maximum values in the ventricles.

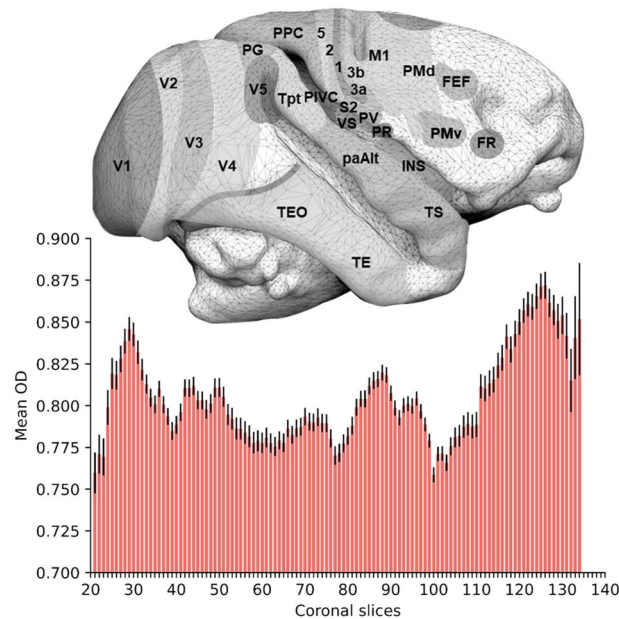


Fig. 5 Mean Orientation Dispersion by slices $N = 10$. A right lateral view of a Saimiri brain surface (top, modified from Royo *et al.* 2021) is aligned to a histogram (bottom) representing the average orientation dispersion (OD) value for grey matter in each coronal slice. Error bars represent the standard error. FEF frontal eye field, FR frontal rostral field, INS insula, M1 primary motor area, PaAlt lateral parakoniocortex, PIVC parieto-insular vestibular cortex, PG inferior parietal lobule, PMv premotor area ventral, PMd premotor area dorsal, PPC posterior parietal cortex, PR presumptive parietal rostral, PV parietal ventral, S2 secondary somatosensory area, 1 2 3a 3b and 5 cytoarchitectonic areas 1 2 3a 3b and 5, TE temporal region, TEO temporo-occipital region, Tpt temporo-parietal region, TS temporalis superior cortex, V1 V2 V3 V4 and V5 visual areas 1 2 3 4 and 5, VS ventral somatosensory.

In order to assess the potential for our measurements to investigate variations in the cortical architecture of the squirrel monkey, we computed a mean OD template from 10 individuals using Advanced Normalisation Tools (ANT) together with the function *buildtemplateparallel.sh*. The mean OD value for the grey matter for each coronal slice was extracted and plotted in Fig. 5. It reveals a clear gradient of variations on the anterior-posterior axis, notably in the occipital and frontal areas. Neurite orientation dispersion being an indicator of the local connective properties of the cortex, this variation indicates the existence of an anterior-posterior gradient of complexity in the frontal area. It might align with brain evolutionary theories of progressive expansion^{49,50} and cytoarchitectural^{51,52} and neuroimaging^{53,54} gradients in the frontal lobes. A similar gradient, posterior-anterior this time, seems to exist in the occipital lobes, albeit, to our knowledge, less documented.

The multishell parameter of our acquisition also allows for using ActiveAx to estimate mean axonal density and diameter. Figure 6 is an example of ActiveAx analysis focusing on a sagittal mid-section of the corpus callosum and demonstrating a dorsoventral gradient of axonal diameter with thicker axons located dorsally. Importantly, DWI-derived estimation of the axonal diameter profile received a lot of criticism⁵⁵. Accordingly the values estimated by ActiveAx were higher than standard values reported post-mortem in other species⁵⁶. While postmortem shrinking can affect values, future investigation on our dataset will allow us to provide true postmortem estimation of the axonal diameter in the squirrel monkey. These post-mortem investigations in the same individuals will allow for the validation of the biological inferences derived from neuroimaging methods.

Despite reaching a staggering resolution of $400\ \mu\text{m}$ *in vivo*, estimation of the orientation and microstructure of connections derived from diffusion-weighted imaging is still not exempt from limitations. In particular, it is essential to highlight that the resolution of myelinated axons (1 to $6\ \mu\text{m}$) leads to partial volume effects that hamper a perfect estimation when a bundle of connections crosses, fans or merges. In spite of this limitation, we provided an estimate of the connections orientation, neurite density and axonal diameter derived from some of the best algorithms currently available for people to explore and potentially improve analyses shortly.

Usage Notes

Our *in vivo* diffusion-weighted imaging dataset of living squirrel monkeys is available on Figshare and a dedicated website regularly updated with additional data and analyses (<http://saimiri.bcblab.com>). We also opened a forum topic for questions and answers (<https://neurostars.org/t/squirrel-monkey-brain-mapping/24110>). This dataset provides future perspectives for anatomists working on brain evolution, who will be able to peer further into the past of primate brain evolution. It will benefit neuroscientists who wish to investigate behavioral models or anatomical systems not available otherwise and neuroimagers who would like to test their new

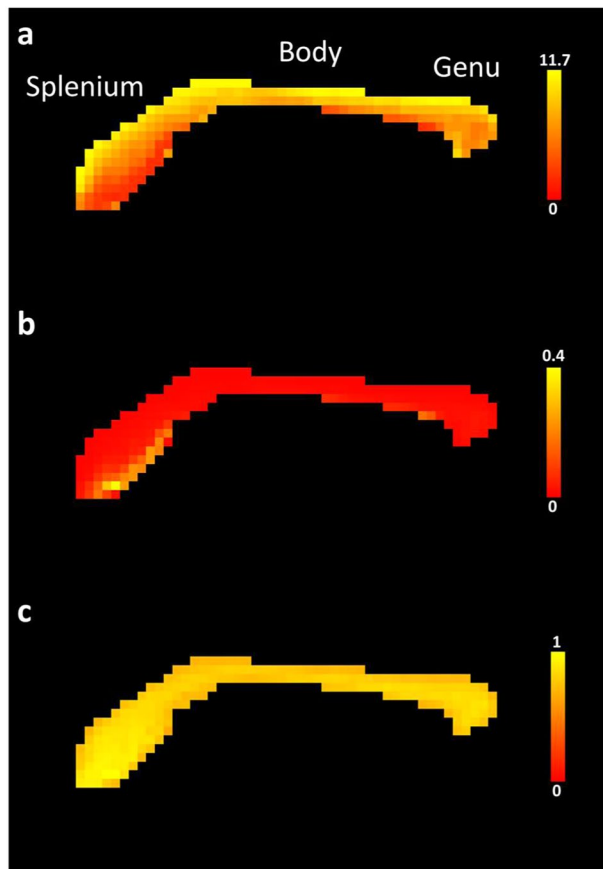


Fig. 6 ActiveAx analysis N = 1. Close-up of sagittal mid-sections of corpus callosum maps for (a) mean axonal diameter in μm , (b) axonal density in axons/ μm^2 and (c) Intra-cellular volume fraction. Mean axonal diameter, axonal density and ICVF correspond to ActiveAx generated files FIT_a, FIT_d and FIT_v respectively.

algorithms. This resource will also permit the refinement of evolutionary mechanisms modeling and potentially allow for identifying future therapeutic targets. We believe this dataset, combined with other resources available to researchers (e.g., PRIME-DE), will permit sharper phylogenetical investigations.

Code availability

All custom codes used to analyze the data are shared on GitHub: https://github.com/Orset-Thomas/Squirrel_monkey_DWI.git.

Received: 4 January 2023; Accepted: 31 March 2023;

Published online: 20 April 2023

References

1. Abee, C. R. Squirrel Monkey (Saimiri spp.) Research and Resources. *ILAR Journal* **41**, 2–9 (2000).
2. Royo, J., Forkel, S. J., Pouget, P. & Thiebaut de Schotten, M. The squirrel monkey model in clinical neuroscience. *Neuroscience & Biobehavioral Reviews* **128**, 152–164 (2021).
3. Anderson, J. R., Awazu, S. & Fujita, K. Squirrel Monkeys (Saimiri sciureus) Choose Smaller Food Arrays: Long-Term Retention, Choice With Nonpreferred Food, and Transposition. *Journal of Comparative Psychology* **118**, 58–64 (2004).
4. Pouydebat, E., Borel, A., Chotard, H. & Frigaszy, D. Hand preference in fast-moving versus slow-moving actions in capuchin, Sapajus spp., and squirrel monkeys, Saimiri sciureus. *Animal Behaviour* **97**, 113–123 (2014).
5. Heiney, S. A. & Blazquez, P. M. Behavioral responses of trained squirrel and rhesus monkeys during oculomotor tasks. *Exp Brain Res* **212**, 409–416 (2011).
6. Overman, W. H., McLain, C., Ormsby, G. E. & Brooks, V. Visual recognition memory in squirrel monkeys. *Animal Learning & Behavior* **11**, 483–488 (1983).
7. Tsujimoto, S. & Sawaguchi, T. Working memory of action: a comparative study of ability to selecting response based on previous action in New World monkeys (Saimiri sciureus and Callithrix jacchus). *Behavioural Processes* **58**, 149–155 (2002).
8. Friedrich, P. *et al.* Imaging evolution of the primate brain: the next frontier? *NeuroImage* **228**, 117685 (2021).
9. Thiebaut de Schotten, M. & Forkel, S. J. The emergent properties of the connected brain. *Science* **378**, 505–510 (2022).
10. Sawaguchi, T. The Size of the Neocortex in Relation to Ecology and Social Structure in Monkeys and Apes. *FPR* **58**, 131–145 (1992).
11. Wang, S. *et al.* Anatomical MRI templates of tree shrew brain for volumetric analysis and voxel-based morphometry. *Journal of Neuroscience Methods* **220**, 9–17 (2013).
12. Takemura, H. & Thiebaut de Schotten, M. Perspectives given by structural connectivity bridge the gap between structure and function. *Brain Struct Funct* **225**, 1189–1192 (2020).

13. Le Bihan, D. & Breton, E. Imagerie de diffusion *in-vivo* par résonance magnétique nucléaire. *Comptes-Rendus de l'Académie des Sciences* **93**, 27–34 (1985).
14. Assaf, Y., Johansen-Berg, H. & Thiebaut de Schotten, M. The role of diffusion MRI in neuroscience. *NMR in Biomedicine* **32**, e3762 (2019).
15. Conturo, T. E. *et al.* Tracking neuronal fiber pathways in the living human brain. *Proceedings of the National Academy of Sciences* **96**, 10422–10427 (1999).
16. Jones, D. K., Simmons, A., Williams, S. C. R. & Horsfield, M. A. Non-invasive assessment of axonal fiber connectivity in the human brain via diffusion tensor MRI. *Magnetic Resonance in Medicine* **42**, 37–41 (1999).
17. Mori, S. *et al.* *In vivo* visualization of human neural pathways by magnetic resonance imaging. *Annals of Neurology* **47**, 412–414 (2000).
18. Basser, P. J., Pajevic, S., Pierpaoli, C., Duda, J. & Aldroubi, A. *In vivo* fiber tractography using DT-MRI data. *Magnetic Resonance in Medicine* **44**, 625–632 (2000).
19. Beaulieu, C. The basis of anisotropic water diffusion in the nervous system – a technical review. *NMR in Biomedicine* **15**, 435–455 (2002).
20. Zhang, H., Schneider, T., Wheeler-Kingshott, C. A. & Alexander, D. C. NODDI: Practical *in vivo* neurite orientation dispersion and density imaging of the human brain. *NeuroImage* **61**, 1000–1016 (2012).
21. Takahashi, M. *et al.* Magnetic resonance microimaging of intraaxonal water diffusion in live excised lamprey spinal cord. *Proceedings of the National Academy of Sciences* **99**, 16192–16196 (2002).
22. D'Arceuil, H. & de Crespigny, A. The effects of brain tissue decomposition on diffusion tensor imaging and tractography. *NeuroImage* **36**, 64–68 (2007).
23. Tovi, M. & Ericsson, A. Measurements of T1 and T2 over time in formalin-fixed human whole-brain specimens. *Acta Radiol* **33**, 400–404 (1992).
24. Thelwall, P. E., Shepherd, T. M., Stanisz, G. J. & Blackband, S. J. Effects of temperature and aldehyde fixation on tissue water diffusion properties, studied in an erythrocyte ghost tissue model. *Magnetic Resonance in Medicine* **56**, 282–289 (2006).
25. Sun, S.-W. *et al.* Differential sensitivity of *in vivo* and *ex vivo* diffusion tensor imaging to evolving optic nerve injury in mice with retinal ischemia. *NeuroImage* **32**, 1195–1204 (2006).
26. Schilling, K. *et al.* Reproducibility and variation of diffusion measures in the squirrel monkey brain, *in vivo* and *ex vivo*. *Magnetic Resonance Imaging* **35**, 29–38 (2017).
27. Zhang, J. *et al.* Longitudinal characterization of brain atrophy of a Huntington's disease mouse model by automated morphological analyses of magnetic resonance images. *NeuroImage* **49**, 2340–2351 (2010).
28. Lerch, J. *et al.* Wanted dead or alive? The tradeoff between *in-vivo* versus *ex-vivo* MR brain imaging in the mouse. *Frontiers in Neuroinformatics* **6**, 6 (2012).
29. Holmes, H. E. *et al.* Comparison of *In Vivo* and *Ex Vivo* MRI for the Detection of Structural Abnormalities in a Mouse Model of Tauopathy. *Frontiers in Neuroinformatics* **11**, 20 (2017).
30. Roebroek, A., Miller, K. L. & Aggarwal, M. *Ex vivo* diffusion MRI of the human brain: Technical challenges and recent advances. *NMR in Biomedicine* **32**, e3941 (2019).
31. Van Essen, D. C. *et al.* The WU-Minn Human Connectome Project: An Overview. *Neuroimage* **80**, 62–79 (2013).
32. Sébille, S. B., Rolland, A.-S., Welter, M.-L., Bardin, E. & Santin, M. D. Post mortem high resolution diffusion MRI for large specimen imaging at 11.7T with 3D segmented echo-planar imaging. *Journal of Neuroscience Methods* **311**, 222–234 (2019).
33. Grier, M. D. *et al.* Ultra-high field (10.5T) diffusion-weighted MRI of the macaque brain. *NeuroImage* **255**, 119200 (2022).
34. Poldrack, R. *et al.* Toward open sharing of task-based fMRI data: the OpenfMRI project. *Frontiers in Neuroinformatics* **7**, 12 (2013).
35. Gorgolewski, K. J. *et al.* NeuroVault.org: a web-based repository for collecting and sharing unthresholded statistical maps of the human brain. *Frontiers in Neuroinformatics* **9**, 8 (2015).
36. Milham, M. P. *et al.* An Open Resource for Non-human Primate Imaging. *Neuron* **100**, 61–74.e2 (2018).
37. Madan, C. R. Scan Once, Analyse Many: Using Large Open-Access Neuroimaging Datasets to Understand the Brain. *Neuroinformatics* **20**, 109–137 (2021).
38. Caruyer, E., Lenglet, C., Sapiro, G. & Deriche, R. Design of multishell sampling schemes with uniform coverage in diffusion MRI. *Magnetic Resonance in Medicine* **69**, 1534–1540 (2013).
39. Dell'Acqua, F., Simmons, A., Williams, S. C. R. & Catani, M. Can spherical deconvolution provide more information than fiber orientations? Hindrance modulated orientational anisotropy, a true-tract specific index to characterize white matter diffusion. *Human Brain Mapping* **34**, 2464–2483 (2013).
40. Guo, F., Leemans, A., Viergever, M. A. & Dell'Acqua, F. & De Luca, A. Generalized Richardson-Lucy (GRL) for analyzing multi-shell diffusion MRI data. *NeuroImage* **218**, 116948 (2020).
41. Alexander, D. C. *et al.* Orientationally invariant indices of axon diameter and density from diffusion MRI. *NeuroImage* **52**, 1374–1389 (2010).
42. Orset, T., Royo, J., Santin, M., Pouget, P. & Thiebaut de Schotten, M. Saimiris 11.7T 400 μ m dMRI multishell *in-vivo* dataset, *Figshare*, <https://doi.org/10.6084/m9.figshare.c.6329417.v1> (2023).
43. Deoni, S. C. L. & Catani, M. Visualization of the deep cerebellar nuclei using quantitative T1 and ρ magnetic resonance imaging at 3 Tesla. *NeuroImage* **37**, 1260–1266 (2007).
44. Thiebaut de Schotten, M. *et al.* A lateralized brain network for visuospatial attention. *Nat Neurosci* **14**, 1245–1246 (2011).
45. Thiebaut de Schotten, M., Dell'Acqua, F., Valabregue, R. & Catani, M. Monkey to human comparative anatomy of the frontal lobe association tracts. *Cortex* **48**, 82–96 (2012).
46. Croxson, P. L., Forkel, S. J., Cerliani, L. & Thiebaut de Schotten, M. Structural Variability Across the Primate Brain: A Cross-Species Comparison. *Cerebral Cortex* **28**, 3829–3841 (2018).
47. Essen, D. C. V. & Dierker, D. L. Surface-Based and Probabilistic Atlases of Primate Cerebral Cortex. *Neuron* **56**, 209–225 (2007).
48. Hill, J. *et al.* Similar patterns of cortical expansion during human development and evolution. *Proceedings of the National Academy of Sciences* **107**, 13135–13140 (2010).
49. Passingham, R. *Understanding the Prefrontal Cortex: Selective Advantage, Connectivity, and Neural Operations*. (Oxford University Press, 2021).
50. Passingham, R. E. & Lau, H. Do we understand the prefrontal cortex? *Brain Struct Funct* <https://doi.org/10.1007/s00429-022-02587-7> (2022).
51. Pandya, D., Petrides, M. & Cipolloni, P. B. *Cerebral Cortex: Architecture, Connections, and the Dual Origin Concept*. (Oxford University Press, 2015).
52. Sanides, F. Functional architecture of motor and sensory cortices in primates in light of a new concept of neocortical evolution. in *The Primate Brain* 137–208 (Appleton-Century-Crofts, 1970).
53. Thiebaut de Schotten, M. *et al.* Rostro-caudal Architecture of the Frontal Lobes in Humans. *Cereb Cortex* **27**, 4033–4047 (2017).
54. Abdallah, M., Zanitti, G. E., Iovene, V. & Wassermann, D. Functional gradients in the human lateral prefrontal cortex revealed by a comprehensive coordinate-based meta-analysis. *eLife* **11**, e76926 (2022).
55. Paquette, M., Eichner, C., Knösche, T. R. & Anwender, A. Axon Diameter Measurements using Diffusion MRI are Infeasible. 2020.10.01.320507 Preprint at <https://doi.org/10.1101/2020.10.01.320507> (2021).
56. Herrera, S. L. *et al.* Axon diameter inferences in the human corpus callosum using oscillating gradient spin echo sequences. *Magnetic Resonance Imaging* **85**, 64–70 (2022).

Acknowledgements

This work was supported by the European Union's Horizon 2020 research and innovation program under the European Research Council (ERC) Consolidator grant agreement N°. 818521 (MTdS, DISCONNECTOME). This study was conducted in the framework of the University of Bordeaux's IdEx "Investments for the Future" program RRI "IMPACT" which received financial support from the French government. We thank the primate facility staff for their valuable help caring for and preparing the animals for the procedures.

Author contributions

Thomas Orset contributed to animal preparation and data acquisition, organized the database, performed data analysis, wrote the first draft of the manuscript, contributed to revision, and read and approved the submitted version. Julie Royo contributed to animal preparation, data acquisition, and manuscript revision, and read and approved the submitted version. Mathieu Santin contributed to MR protocol design, MR protocol design, and data acquisition, wrote a section of the manuscript, contributed to manuscript revision, and read and approved the submitted version. Pierre Pouget contributed to the conception and design of the study, contributed to manuscript revision, read and approved the submitted version. Michel Thiebaut de Schotten contributed to the conception and design of the study, contributed to manuscript revision, provided funding, and read and approved the submitted version.

Competing interests

The authors declare that the research was conducted in the absence of any commercial or financial relationships that could be construed as a potential conflict of interest.

Additional information

Correspondence and requests for materials should be addressed to T.O.

Reprints and permissions information is available at www.nature.com/reprints.

Publisher's note Springer Nature remains neutral with regard to jurisdictional claims in published maps and institutional affiliations.



Open Access This article is licensed under a Creative Commons Attribution 4.0 International License, which permits use, sharing, adaptation, distribution and reproduction in any medium or format, as long as you give appropriate credit to the original author(s) and the source, provide a link to the Creative Commons license, and indicate if changes were made. The images or other third party material in this article are included in the article's Creative Commons license, unless indicated otherwise in a credit line to the material. If material is not included in the article's Creative Commons license and your intended use is not permitted by statutory regulation or exceeds the permitted use, you will need to obtain permission directly from the copyright holder. To view a copy of this license, visit <http://creativecommons.org/licenses/by/4.0/>.

© The Author(s) 2023